Local Berry Phase Signatures of Bilayer Graphene in Intervalley Quantum Interference

Yu Zhang,[1,†] Ying Su,[2,†] and Lin He[1,*]

[1]*Center for Advanced Quantum Studies, Department of Physics, Beijing Normal University, Beijing 100875, People's Republic of China*

[2]*Theoretical Division, T-4 and CNLS, Los Alamos National Laboratory, Los Alamos, New Mexico 87545, USA*

(Received 13 May 2020; accepted 20 August 2020; published 10 September 2020)

Chiral quasiparticles in Bernal-stacked bilayer graphene have valley-contrasting Berry phases of $\pm 2\pi$. This nontrivial topological structure, associated with the pseudospin winding along a closed Fermi surface, is responsible for various novel electronic properties. Here we show that the quantum interference due to intervalley scattering induced by single-atom vacancies or impurities provides insights into the topological nature of the bilayer graphene. The scattered chiral quasiparticles between distinct valleys with opposite chirality undergo a rotation of pseudospin that results in the Friedel oscillation with wavefront dislocations. The number of dislocations reflects the information about pseudospin texture and hence can be used to measure the Berry phase. As demonstrated both experimentally and theoretically, the Friedel oscillation, depending on the single-atom vacancy or impurity at different sublattices, can exhibit $N = 4$, 2, or 0 additional wavefronts, characterizing the 2π Berry phase of the bilayer graphene. Our results provide a comprehensive study of the intervalley quantum interference in bilayer graphene and can be extended to multilayer graphene, shedding light on the pseudospin physics.

DOI: 10.1103/PhysRevLett.125.116804

The Berry phase plays a very important role in determining the electronic dynamics and topological properties of materials [1–11]. In the low-energy band structures of graphene systems, the nonzero Berry phase is associated with the pseudospin winding [1–6,12–16]. In single-layer graphene (SLG), the pseudospin rotates by 2π along a closed Fermi surface that corresponds to the Berry phase $\gamma = \pi$, which is responsible for the Klein tunneling and the half-integer quantum Hall effect [12–16]. In Bernal-stacked bilayer graphene (BLG), the pseudospin rotates by 4π along a closed Fermi surface and the Berry phase is $\gamma = 2\pi$. This leads to exotic electronic properties, such as the anti-Klein tunneling and integer quantum Hall effect with a peculiar absent zero Hall conductance plateau, in the BLG [1–6].

The direct measurement of the Berry phase is desirable to reveal the topological structure of materials and it is usually realized by using magnetic fields [1,2,12–15]. Alternatively, probing the pseudospin winding also provides the information about the Berry phase of graphene. In the presence of time-reversal symmetry, the pseudospin texture has opposite chirality at distinct valleys [7]. As a consequence, the scattered chiral quasiparticle between two distinct valleys undergoes a rotation of pseudospin, which thus gives rise to the quantum interference that encodes the information about the pseudospin winding and the Berry phase [7,17]. Very recently, it has been shown that the Berry phase of the SLG can be measured from the wavefront dislocations in the charge density modulation, i.e., the Friedel oscillation, induced by a single-atom impurity. The number of dislocations satisfies $2\pi N = 4\gamma$, from which the $N = 2$ additional wavefronts in the vicinity of a single-atom impurity are a signature of the $\gamma = \pi$ Berry phase in the SLG [7]. This experiment provides an efficient method to measure the Berry phase without using external magnetic fields.

In this Letter, we focus on the Bernal-stacked BLG whose topological structure is very different from the SLG. By using the scanning tunneling microscopy (STM), we measure the pseudospin winding and the Berry phase of the BLG from the wavefront dislocations in the Friedel oscillations around individual single-atom vacancy (a carbon atom of graphene is missing) and impurity (a H atom chemisorbed on a carbon atom of graphene). The BLG exhibits $N = 4$, 2, or 0 additional wavefronts for a single-atom vacancy or impurity at different sublattices, exhibiting very different behavior from the SLG where the numbers of additional wavefronts are sublattice independent [7]. To understand the observed peculiar phenomena, we simulate the intervalley quantum interference in the BLG with a single-atom vacancy or impurity by the tight-binding model and continuum model. Our theoretical simulation shows that the total number of dislocations in the two layers is $N = 4$ because the Berry phase $\gamma = 2\pi$ of the BLG. However, the number of dislocations in the top layer can be $N = 4$, 2, or 0, depending on the single-atom vacancy or impurity at different sublattices, as observed in our experiment. Furthermore, this result is extended to the multilayer graphene system.

In our experiments, we directly synthesize multilayer graphene on Ni foils by using a chemical vapor deposition

(CVD) method [18–20] (see methods and Fig. S1 [21]). A high density of single-atom vacancy can be clearly observed in STM images (Fig. S2 [21]). The H atoms are introduced on the surface of graphene via a H_2 plasma after the synthesis of graphene [22] (see methods of the Supplemental Material [21]). To identify the decoupled Bernal-stacked BLG regions, we carry out both the STM and scanning tunneling spectroscopy (STS) measurements. As observed in the Bernal-stacked BLG, the atomic-resolution STM images of the vacancy or impurity-free regions exhibit a triangular contrast due to the sublattice asymmetry generated by the two adjacent graphene layers [Figs. 1(a)–1(c)] [23]. The high-magnetic-field STS spectra show well-defined Landau quantization of massive Dirac fermions (Fig. S3 [21]), as observed previously in the Bernal-stacked BLG [23–25], demonstrating that the studied topmost BLG behaves as the pristine Bernal-stacked BLG.

Figures 1(a)–1(c) show three representative STM images of the BLG with a single-atom vacancy or impurity at different sublattices. The characteristic $\sqrt{3} \times \sqrt{3}R30°$ interference patterns induced by the single-atom vacancy or impurity can be clearly observed [19,20,22,26–30]. In the STM measurements, it is easy to distinct single-atom vacancy and the single-atom impurity because that there is a little Jahn-Teller distortion around the single-atom vacancy [19,20]. In the Bernal-stacked BLG, the B sublattices of the topmost graphene sheet are located exactly on top of the A' sublattices of the underlying graphene layer. The visible atoms of the Bernal-stacked BLG are the A sublattice of the topmost layer in the STM images [31,32]. According to previous studies [19,20,22,26–30] and our tight binding calculations shown in Figs. 2(a)–2(c), we can find out that the single-atom vacancy or impurity is located at the center of the tripod shape (black dotted outline). Therefore, the atomic sites of the vacancy or impurity can be unambiguously identified by overlying the lattice structures onto the enlarged STM images [Figs. 1(d)–1(f)]. The atomic structures can be further precisely determined via the apparent heights of the vacancy or impurity-induced protrusions in the STM images [20] and orientations of the tripod shapes with respect to the directions of the nearest σ bonds of the vacancy or impurity (Figs. S4 and S5 [21]). According to our experiment, a single-atom vacancy is located at the B' (A) sublattice of the BLG in Fig. 1(a) [1(c)] and a single-atom impurity is located on the B sublattice of the BLG in Fig. 1(b), as specified in Figs. 1(g)–1(i), respectively.

The fast Fourier transform (FFT) of the STM images in Figs. 1(a)–1(c) are shown in Figs. 1(j)–1(l), respectively. The bright spots at the reciprocal lattice of the BLG are connected by yellow dashed hexagon. At the center of the hexagon, the ring with the radius of $2q_F$ (q_F is the Fermi wave vector) is induced by the intravalley scattering [33–35]. Such a feature is, however, suppressed in the SLG due to the π rotation of pseudospin and can be used to distinguish the BLG from the SLG [33–36]. The additional bright spots marked by a green dashed hexagon are due to

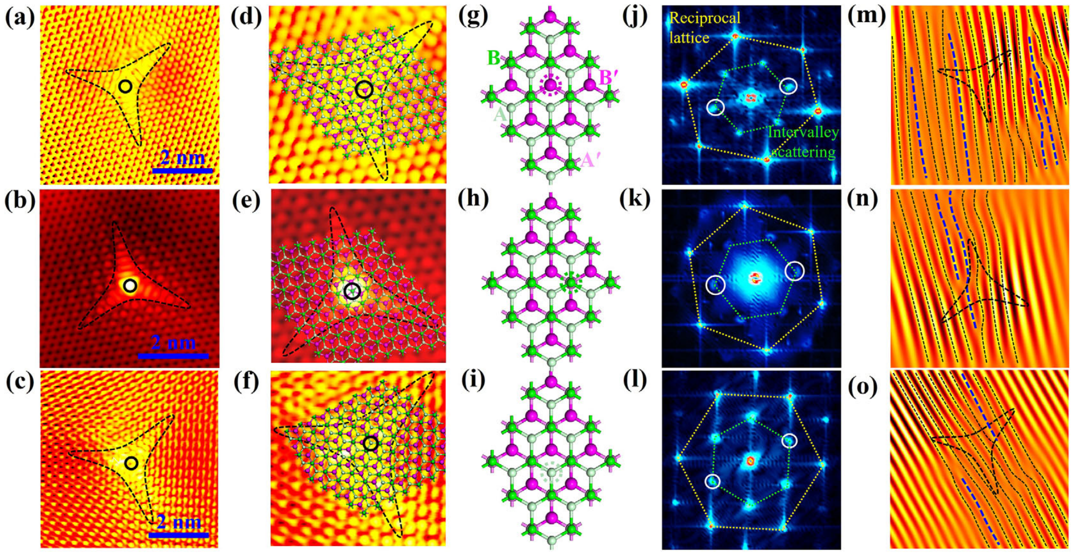

FIG. 1. (a)–(c) The topography STM images of the individual single-atom vacancy (a), (c) and impurity (b) in the decoupled BLG. The single-atom vacancies or impurities (black circles) locate at the center of the tripod shapes. (d)–(f) Atomic structures of BLG overlying onto the enlarged STM images. (g)–(i) Atomic structures of the BLG with the single-atom vacancy or impurity at the B', B, and A sublattices, respectively. The locations of the vacancy or impurity are marked by the dotted circles. (j)–(l) FFT of panels (a)–(c). The outer and inner hexangular spots, linking by the yellow and green lines, correspond to the reciprocal lattice of graphene and the intervalley scattering, respectively. (m)–(o) FFT-filtered images of panels (a)–(c) along the direction of intervalley scattering marked by white circles in panels (j)–(l), which exhibit $N = 4$, 2, and 0 additional wavefronts (blue dashed lines), respectively.

the intervalley scattering [33–37]. To show the intervalley scattering induced Friedel oscillations of charge density, we do the inverse FFT of the filtered bright spots enclosed by the white circles in Figs. 1(j)–1(l), and the corresponding FFT-filtered images are given in Figs. 1(m)–1(o). The results for the intervalley scattering in the other two directions are related by a C_3 rotation (Figs. S6–S8 [21]), which also show the same features. According to the experimental results in Figs. 1(m)–1(o), there are apparent $N = 4$, 2, and 0 additional wavefronts for the single-atom vacancy or impurity at the B', B, and A sublattices of the BLG, respectively. The additional wavefronts around the vacancy or impurity-induced intervalley interference are quite robust even with considering the effects of the tip gating. The STM tip can generate a slight band bending beneath the tip [5,38,39], which is not expected to affect the topological structure in the BLG, therefore, is not expected to affect the additional wavefronts around the single-atom vacancy or impurity.

To understand our experimental results, we first carry out the tight binding simulations to reproduce the wavefront dislocations induced by intervalley scattering around single-atom vacancies of the Bernal-stacked BLG (see Supplemental Material for details [21]). We consider a BLG flake with 100 × 100 unit cells and periodic boundary conditions, and we locate a single-atom vacancy at the center. Because the STM measures mainly the charge density in the top layer, Figs. 2(a)–2(c) show the simulated charge densities in the top layer for the single-atom vacancy at the B', B, and A sublattices of the BLG, as schematically shown in Figs. 1(g)–1(i). Here we fix the Fermi energy $\omega = 30$ meV in the numerical simulation. The FFT of the charge densities in Figs. 2(a)–2(c) are exhibited as insets. For the intervalley scattering in the direction specified by the white circles in the insets of Figs. 2(a)–2(c), the filtered inverse FFT results in the charge density oscillations in Figs. 2(d)–2(f). Here the numbers of additional wavefronts are $N = 4$, 2, and 0 for the single-atom vacancy at the B', B, and A sublattices, respectively, and the results in the other two directions exhibit the same features. Obviously, our theoretical results are well consistent with the experimental results.

To gain further insights into the peculiar wavefront dislocations in the BLG, we study the single-atom vacancy or impurity induced intervalley quantum interference based on the low-energy continuum model of the BLG [6]

$$\mathscr{H}_{\boldsymbol{K}_\xi+\boldsymbol{q}} = -\frac{v_F^2 q^2}{t_\perp}\begin{pmatrix} 0 & e^{2\xi i\theta_{\boldsymbol{q}}} \\ e^{-2\xi i\theta_{\boldsymbol{q}}} & 0 \end{pmatrix}, \tag{1}$$

which is expressed in the basis of $\{A, B'\}$. Here $\xi = \pm$ is the valley index, v_F is the Fermi velocity, $t_\perp \approx 0.4$ eV is the nearest neighboring interlayer hopping [40], and $\theta_{\boldsymbol{q}}$ is the polar angle of electrons with the momentum $\boldsymbol{q}$ [see Fig. 3(c)]. The eigenvalues of the Hamiltonian are $E^{\pm}_{\boldsymbol{K}_\xi+\boldsymbol{q}} = \pm v_F^2 q^2/t_\perp$, which yields the band structure in Fig. 3(a). The corresponding eigenvectors are $|\psi^{\pm}_{\boldsymbol{K}_\xi+\boldsymbol{q}}\rangle = (1/\sqrt{2})\times \binom{1}{\mp e^{-2\xi i\theta_{\boldsymbol{q}}}}$, which defines the pesudospin

$$\langle\psi^{\pm}_{\boldsymbol{K}_\xi+\boldsymbol{q}}|\boldsymbol{\sigma}|\psi^{\pm}_{\boldsymbol{K}_\xi+\boldsymbol{q}}\rangle = (\mp \cos 2\xi\theta_{\boldsymbol{q}}, \pm \sin 2\xi\theta_{\boldsymbol{q}}, 0), \tag{2}$$

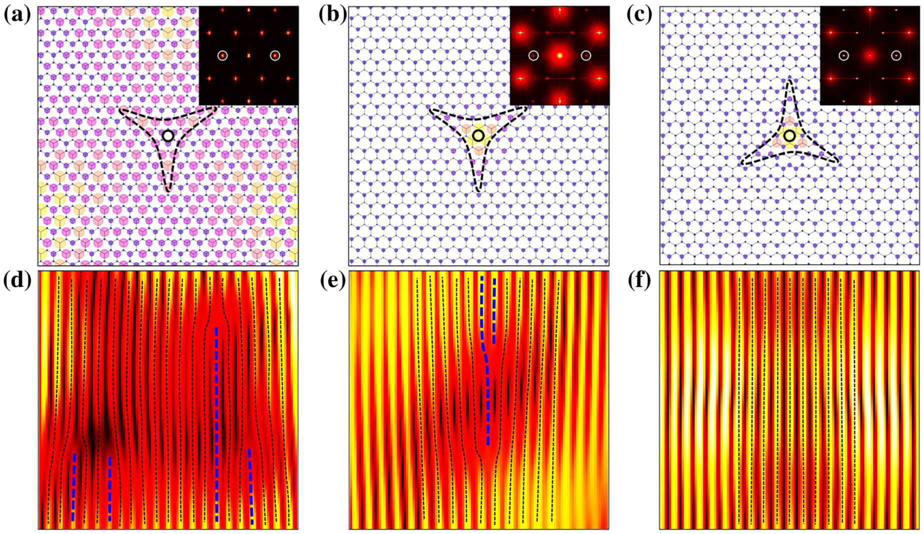

FIG. 2. (a)–(c) Simulated charge density in the top layer of the BLG with a single-atom vacancy at the B', B, and A sublattices, respectively. The single-atom vacancy (black circles) is at the center of the tripod-shaped charge density (black dotted outlines). Here the charge density is calculated at the energy of 30 meV and is represented by the spots whose size is proportional to the charge density. The FFT of the charge density is shown as insets. (d)–(f) Charge density oscillations due to the intervalley quantum interference are obtained from the filtered FFT enclosed by white circles in (a)–(c), respectively. For the single-atom vacancy located at the three distinct sublattices in (a)–(c), there are $N = 4$, 2, and 0 additional wavefronts marked by blue dashed lines.

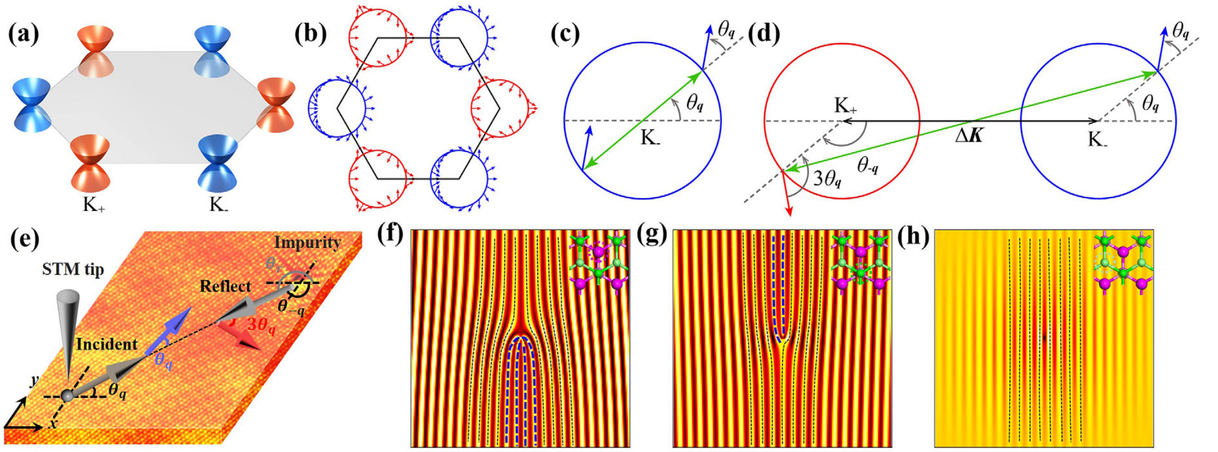

FIG. 3. (a) Low-energy band structures around the Brillouin zone corners of the BLG. (b) Pseudospin textures along the Fermi surfaces in the BLG. (c) Schematic intravalley scattering in the BLG. (d) Schematic intervalley scattering in the BLG. The pseudospin rotates by $4\theta_q$ in the intervalley scattering. (e) The real space representation of the intervalley backward scattering in panel (d). The red and blue arrows denote the pseudospins of reflected and incident quasiparticles from the K_+ and K_- valleys, respectively. (f)–(h) Charge density oscillations due to the intervalley scattering are calculated from the low-energy continuum model and projected onto the top layer of the BLG. For the single-atom vacancy or impurity at the B', B, and A sublattices, the charge density oscillations at the energy of 30 meV exhibit $N = 4$, 2, and 0 additional wavefronts, as marked by blue dashed lines.

where $\boldsymbol{\sigma}$ is the vector of Pauli matrices acting on the sublattice space. Figure 3(b) shows the pseudospin texture on the Fermi surfaces. The pseudospin rotates by 4π along a closed Fermi surface that yields the $W = 2$ winding number and the $\gamma = W\pi = 2\pi$ Berry phase in the BLG.

The intravalley and intervalley scattering processes in the BLG are sketched in Figs. 3(c) and 3(d), respectively. The intravalley scattering leaves the pseudospin unchanged [Fig. 3(c)], which can be negligible in the quantum interference. In contrast, the intervalley scattering rotates the pseudospin by $4\theta_{\boldsymbol{q}}$ [Fig. 3(d)]. The schematic representation of the intervalley scattering process in real space is shown in Fig. 3(e). At a given STM tip position, the amplitude of the Friedel oscillation is governed by the interference of the electronic waves in the incident and reflected processes. Here we parametrize the tip orientation relative to the vacancy or impurity by the polar angle $\theta_{\boldsymbol{r}} = \theta_{\boldsymbol{q}} + \pi$. The locking of $\theta_{\boldsymbol{r}}$ and $\theta_{\boldsymbol{q}}$ indicates that circling the tip along a path enclosing the vacancy or impurity is equivalent to rotate $\theta_{\boldsymbol{q}}$ along a closed Fermi surface. Because the pseudospin texture in Eq. (2) is originated from the phase difference between the two components of the eigenvector, the incident and reflected electronic waves have a phase difference of $4\theta_{\boldsymbol{q}}$, same as the rotation angle of the pseudospin in the intervalley scattering. Therefore, the phase shift accumulated over a closed scanning path enclosing the vacancy or impurity satisfies $\int_0^{2\pi} 4d\theta_{\boldsymbol{q}} = 2\pi N = 4\gamma$. The vacancy or impurity at $\boldsymbol{r} = 0$ can be regarded as a phase singularity [41,42] and the total number of additional wavefronts due to the phase shift is $N = 4$ for the $\gamma = 2\pi$ Berry phase of the BLG.

However, the STM images, which mainly reflect the electronic distributions of the topmost graphene sheet in the BLG, are not necessary to show $N = 4$ additional wavefronts. In fact, the intervalley scattering induced modulation of charge densities projected onto the top and bottom graphene layers in the BLG are

$$\Delta\rho_t(\boldsymbol{r},\omega,\Delta\boldsymbol{K}) = \Delta\rho_A(r,\omega)\cos(\Delta\boldsymbol{K}\cdot\boldsymbol{r} + N_A\theta_{\boldsymbol{r}}) + \Delta\rho_B(r,\omega)\cos(\Delta\boldsymbol{K}\cdot\boldsymbol{r} + N_B\theta_{\boldsymbol{r}}), \tag{3}$$

$$\Delta\rho_b(\boldsymbol{r},\omega,\Delta\boldsymbol{K}) = \Delta\rho_{A'}(r,\omega)\cos(\Delta\boldsymbol{K}\cdot\boldsymbol{r} + N_{A'}\theta_{\boldsymbol{r}}) + \Delta\rho_{B'}(r,\omega)\cos(\Delta\boldsymbol{K}\cdot\boldsymbol{r} + N_{B'}\theta_{\boldsymbol{r}}), \tag{4}$$

where ω denotes the Fermi energy and $\Delta\boldsymbol{K}$ is the momentum difference from a given $\boldsymbol{K}_+$ point to the nearest neighboring $\boldsymbol{K}_-$ point in the intervalley scattering process, as shown in Fig. 3(d). $\Delta\rho_X(r,\omega)$ and $\cos(\Delta K\cdot\boldsymbol{r} + N_X\theta_{\boldsymbol{r}})$ ($X = A, B, A'$, or B') describe the modulation of charge density projected onto the X sublattice in the radial and transverse directions, respectively (see Supplemental Material for details [21]). The charge density modulated by the trigonometric function changes signs for $|N_X|$ times when scanning around the vacancy or impurity with $\theta_{\boldsymbol{r}}$ rotated by 2π, thus resulting in the emergence of N_X additional wavefronts in the Friedel oscillation at the X sublattice.

Now we focus on the low-energy limit, $\omega \ll t_\perp$, where $\Delta\rho_A \gg \Delta\rho_B$ and $\Delta\rho_{B'} \gg \Delta\rho_{A'}$ because the electronic states of the lowest two bands are mainly from the A and B' sublattices. As a consequence, the wavefront dislocations in the top and bottom layers are expected to be determined by $|N_A|$ and $|N_{B'}|$ respectively. According to the calculation, we obtain $N_A = 4$ and $N_{B'} = 0$, $N_A = 2$ and $N_{B'} = -2$, and $N_A = 0$ and $N_{B'} = -4$, for the single-atom vacancy or impurity at the B', B, and A sublattice, respectively (see Supplemental Material for details [21]). Indeed, there are $N = 4$, 2, and 0 additional wavefronts in the top layer of the BLG, as shown in Figs. 3(f)–3(h). The numbers of additional wavefronts are consistent with the experiments and tight-binding results, while the locations of the additional wavefronts are different, which may result from the filter of the FFT image and finite size effect in the calculation. Now we can provide a comprehensive understanding of our experiments. The robust $N = |N_A| + |N_{B'}| = 4$ additional wavefronts are expected to be observed in the intervalley interference patterns in the BLG. However, the vacancy or impurity efficiently redistributes the numbers of additional wavefronts in the two graphene layers. Therefore, we obtain $N = 4$, 2, and 0 additional wavefronts in the top layer of the BLG in our experiment. Furthermore, this result can be extended to the multilayer graphene systems. For example, in the ABC-stacked trilayer graphene, the $\gamma = 3\pi$ Berry phase results in $N = 6, 4, 2, 0$ additional wavefronts for the single-atom vacancy or impurity at different sublattices (see Supplemental Material [21]). More generally, the $\gamma = l\pi$ Berry phase of rhombohedral l-layer graphene is expected to show $N = 2l,\ 2l - 2, \ldots, 0$ additional wavefronts for the single-atom vacancy or impurity at different sublattices.

In summary, the intervalley scattering induced by single-atom vacancies or impurities in Bernal-stacked BLG is systemically studied via the STM measurements. The quantum interference due to intervalley scattering is manifested by the wavefront dislocations in the Friedel oscillation that can be used to measure the Berry phase. Our work provides a comprehensive measurement of the intervalley quantum interference and the Berry phase of the BLG. The method of measuring Berry phase from wavefront dislocations can be applied to multilayer graphene systems and other 2D materials.

This work was supported by the National Natural Science Foundation of China (Grants No. 11974050 and No. 11674029). L. H. also acknowledges support from the National Program for Support of Top-notch Young Professionals, support from “the Fundamental Research Funds for the Central Universities”, and support from the “Chang Jiang Scholars Program”. Y. S. was supported by the U.S. Department of Energy through the Los Alamos National Laboratory LDRD program, and was supported by the Center for Non-linear Studies at LANL.

---

[*] Corresponding author.
helin@bnu.edu.cn

[†] These authors contributed equally to this work.

[1] K. S. Novoselov, E. Mccann, S. V. Morozov, V. I. Fal'ko, M. I. Katsnelson, U. Zeitler, D. Jiang, F. Schedin, and A. K. Geim, Unconventional quantum Hall effect and Berry's phase of 2π in bilayer graphene, Nat. Phys. **2**, 177 (2006).

[2] Y. Shimazaki, M. Yamamoto, I. V. Borzenets, K. Watanabe, T. Taniguchi, and S. Tarucha, Generation and detection of pure valley current by electrically induced Berry curvature in bilayer graphene, Nat. Phys. **11**, 1032 (2015).

[3] G. M. Rutter, S. Jung, N. N. Klimov, D. B. Newell, N. B. Zhitenev, and J. A. Stroscio, Microscopic polarization in bilayer graphene, Nat. Phys. **7**, 649 (2011).

[4] A. Varlet, M.-H. Liu, and V. Krueckl, D. Bischoff, P. Simonet, K. Watanabe, T. Taniguchi, K. Richter, K. Ensslin, and T. Ihn, Fabry-Pérot Interference in Gapped Bilayer Graphene with Broken Anti-Klein Tunneling, Phys. Rev. Lett. **113**, 116601 (2014).

[5] Y.-W. Liu, Z. Hou, S.-Y. Li, Q.-F. Sun, and L. He, Movable Valley Switch Driven by Berry Phase in Bilayer-Graphene Resonators, Phys. Rev. Lett. **124**, 166801 (2020).

[6] C. Park and N. Marzari, Berry phase and pseudospin winding number in bilayer graphene, Phys. Rev. B **84**, 205440 (2011).

[7] C. Dutreix, H. González-Herrero, I. Brihuega, M. I. Katsnelson, C. Chapelier, and V. T. Renard, Measuring the Berry phase of graphene from wavefront dislocations in Friedel oscillations, Nature (London) **574**, 219 (2019).

[8] M. V. Berry, Quantal phase factors accompanying adiabatic changes, Proc. R. Soc. A **392**, 45 (1984).

[9] D. J. Thouless, M. Kohmoto, M. P. Nightingale, and M. Nijs, Quantized Hall Conductance in a Two-Dimensional Periodic Potential, Phys. Rev. Lett. **49**, 405 (1982).

[10] R. Resta, Macroscopic polarization in crystalline dielectrics: The geometric phase approach, Rev. Mod. Phys. **66**, 899 (1994).

[11] D. Xiao, M. Chang, and Q. Niu, Berry phase effects on electronic properties, Rev. Mod. Phys. **82**, 1959 (2010).

[12] K. S. Novoselov, A. K. Geim, S. V. Morozov, D. Jiang, M. I. Katsnelson, I. V. Grigorieva, S. V. Dubonos, and A. A. Firsov, Two-dimensional gas of massless Dirac fermions in graphene, Nature (London) **438**, 197 (2005).

[13] Y. Zhang, Y. Tan, H. L. Stormer, and P. Kim, Experimental observation of the quantum Hall effect and Berry's phase in graphene, Nature (London) **438**, 201 (2005).

[14] D. L. Miller, K. D. Kubista, G. M. Rutter, and P. Kim, Observing the quantization of zero mass carriers in graphene, Science **324**, 924 (2009).

[15] A. F. Young and P. Kim, Quantum interference and Klein tunnelling in graphene heterojunctions, Nat. Phys. **5**, 222 (2009).

[16] G. P. Mikitik and Y. V. Sharlai, The Berry phase in graphene and graphite multilayers, Fiz. Nizk. Temp. **34**, 1012 (2008).

[17] J. Friedel, The distribution of electrons round impurities in monovalent metals, Philos. Mag. **43**, 153 (1952).

[18] H. Yan, C. Liu, K. Bai *et al.*, Electronic structures of graphene layers on a metal foil: The effect of atomic-scale defects, Appl. Phys. Lett. **103**, 143120 (2013).

[19] Y. Zhang, S.-Y. Li, H. Huang, W.-T. Li, J.-B. Qiao, W.-X. Wang, L.-J. Yin, K.-K. Bai, W. Duan, and L. He, Scanning Tunneling Microscopy of the π Magnetism of a Single Carbon Vacancy in Graphene, Phys. Rev. Lett. **117**, 166801 (2016).

[20] Y. Zhang, F. Gao, S. Gao, and L. He, Tunable magnetism of a single-carbon vacancy in graphene, Sci. Bull. **65**, 194 (2020).

[21] See Supplemental Material at http://link.aps.org/supplemental/10.1103/PhysRevLett.125.116804 for methods, more STM images, STS spectra, and details of the analysis.

[22] Y. Zhang, Q. Guo, S. Li, and L. He, Nanoscale probing of broken-symmetry states in graphene induced by individual atomic impurities, Phys. Rev. B **101**, 155424 (2020).

[23] L.-J. Yin, S.-Y. Li, J.-B. Qiao, J.-C. Nie, and L. He, Landau quantization in graphene monolayer, Bernal bilayer, and Bernal trilayer on graphite surface, Phys. Rev. B **91**, 115405 (2015).

[24] L.-J. Yin, H. Jiang, J.-B. Qiao, and L. He, Direct imaging of topological edge states at a bilayer graphene domain wall, Nat. Commun. **7**, 11760 (2016).

[25] M. O. Goerbig, Electronic properties of graphene in a strong magnetic field, Rev. Mod. Phys. **83**, 1193 (2011).

[26] M. M. Ugeda, I. Brihuega, F. Guinea, and J. M. Gómez-Rodríguez, Missing Atom as a Source of Carbon Magnetism, Phys. Rev. Lett. **104**, 096804 (2010).

[27] H. González-Herrero, J. M. Gómez-Rodríguez, P. Mallet, M. Moaied, J. J. Palacios, C. Salgado, M. M. Ugeda, J.-Y. Veuillen, F. Yndurain, and I. Brihuega, Atomic-scale control of graphene magnetism by using hydrogen atoms, Science **352**, 437 (2016).

[28] J. Mao, Y. Jiang, D. Moldovan, G. Li, K. Watanabe, T. Taniguchi, M. R. Masir, F. M. Peeters, and E. Y. Andrei, Realization of a tunable artificial atom at a supercritically charged vacancy in graphene, Nat. Phys. **12**, 545 (2016).

[29] Y. Jiang, P. Lo, D. May, G. Li, G.-Y. Guo, F. B. Anders, T. Taniguchi, K. Watanabe, J. Mao, and E. Y. Andrei, Inducing Kondo screening of vacancy magnetic moments in graphene with gating and local curvature, Nat. Commun. **9**, 2349 (2018).

[30] O. V. Yazyev and L. Helm, Defect-induced magnetism in graphene, Phys. Rev. B **75**, 125408 (2007).

[31] P. Xu, Y. Yang, D. Qi, S. D. Barber, J. K. Schoelz, M. L. Ackerman, L. Bellaiche, and P. M. Thibado, Electronic transition from graphite to graphene via controlled movement of the top layer with scanning tunneling microscopy, Phys. Rev. B **86**, 085428 (2012).

[32] D. Tomanek, S. G. Louie, H. J. Mamin, D. W. Abraham, R. E. Thomson, E. Ganz, and J. Clarke, Theory and observation of highly asymmetric atomic structure in scanning-tunneling-microscopy images of graphite, Phys. Rev. B **35**, 7790 (1987).

[33] C. Bena, Effect of a Single Localized Impurity on the Local Density of States in Monolayer and Bilayer Graphene, Phys. Rev. Lett. **100**, 076601 (2008).

[34] I. Brihuega, P. Mallet, C. Bena, S. Bose, C. Michaelis, L. Vitali, F. Varchon, L. Magaud, K. Kern, and J. Y. Veuillen, Quasiparticle Chirality in Epitaxial Graphene Probed at the Nanometer Scale, Phys. Rev. Lett. **101**, 206802 (2008).

[35] P. Mallet, I. Brihuega, S. Bose, M. M. Ugeda, J. M. Gómez-Rodríguez, K. Kern, and J. Y. Veuillen, Role of pseudospin in quasiparticle interferences in epitaxial graphene probed by high-resolution scanning tunneling microscopy, Phys. Rev. B **86**, 045444 (2012).

[36] C. Dutreix and M. I. Katsnelson, Friedel oscillations at the surfaces of rhombohedral N-layer graphene, Phys. Rev. B **93**, 035413 (2016).

[37] G. M. Rutter, J. N. Crain, N. P. Guisinger, T. Li, P. N. First, and J. A. Stroscio, Scattering and interference in epitaxial graphene, Science **317**, 219 (2007).

[38] N. M. Freitag, T. Reisch, L. A. Chizhova *et al.*, Large tunable valley splitting in edge-free graphene quantum dots on boron nitride, Nat. Nanotechnol. **13**, 392 (2018).

[39] N. M. Freitag, L. A. Chizhova, and P. Nemes-Incze, Electrostatically confined monolayer graphene quantum dots with orbital and valley splittings, Nano Lett. **16**, 5798 (2016).

[40] A. H. Castro Neto, F. Guinea, N. M. R. Peres, K. S. Novoselov, and A. K. Geim, The electronic properties of graphene, Rev. Mod. Phys. **81**, 109 (2009).

[41] J. F. Nye and M. V. Berry, Dislocations in wave trains, Proc. R. Soc. A **336**, 165 (1974).

[42] M. Mecklenburg and B. Regan, Spin and the Honeycomb Lattice: Lessons from Graphene, Phys. Rev. Lett. **106**, 116803 (2011).